Spatiotemporal characterization of the laser-induced plasma plume in simulated Martian conditions

D. S. Vogt[1], S. Schröder[1], S. Frohmann[1], P. B. Hansen[1], F. Seel[1,3], M. Gensch[1,2], H.-W. Hübers[1,3]
1) Institute of Optical Sensor Systems, German Aerospace Center (DLR), Berlin, Germany
2) Department of Physics, Technical University of Berlin, Berlin, Germany
3) Department of Physics, Humboldt University of Berlin, Berlin, Germany

Corresponding author:
Dr. David S. Vogt
DLR Institute of Optical Sensor Systems
Rutherfordstraße 2
12489 Berlin, Germany
+49 30 67055-427
david.vogt@dlr.de

Abstract

With ChemCam on NASA's Curiosity rover, SuperCam on NASA's Perseverance rover, and MarSCoDe on the Zhurong rover of the China National Space Administration, there are currently three instruments on Mars that employ laser-induced breakdown spectroscopy (LIBS) to analyze the chemical composition of Martian rocks and soils. With more than 880,000 LIBS measurements on Mars by ChemCam alone, the LIBS technique has been proven to be uniquely qualified for the in-situ robotic exploration of planetary surfaces. Since the laser-induced plasma exhibits a complex spatiotemporal evolution that has a significant impact on the recorded LIBS spectra, fundamental investigations of the plasma propagation and the spatial distributions of the plasma emissions can provide important insight that can help to improve the analysis of Martian LIBS spectra. Here we present first results from our LIBS plasma imaging setup, which allows us to spatially and temporally resolve the spectral emissions from the laser-induced plasma in simulated Martian atmospheric conditions. Investigating a calcium sulfate sample, we find that the commonly applied assumption of a nearly isothermal and homogeneous plasma with a colder outer layer is not sufficient to describe the laser-induced plasma on Mars. Instead, different spectral features show unique spatial distributions that suggest a strong influence of the outgoing shock wave. After plasma formation, the plasma center is found to rapidly become colder and more rarefied than the outer plasma regions. Molecular emissions are found to originate in this cold plasma center.

Keywords: LIBS, Plasma Imaging, Spectroscopy, Mars

1 Introduction

Laser-induced breakdown spectroscopy (LIBS) has been of great interest for robotic planetary exploration in the last two decades because of its unique qualities as a contact-free technique that is able to analyze the geochemical composition of planetary surfaces from stand-off distances [1]. It uses a focused laser pulse to ablate material from a sample surface, generating a bright plasma plume that emits light with a characteristic spectrum of atomic, ionic, and molecular spectral features [2]. The ChemCam instrument suite onboard the Curiosity rover of NASA's Mars Science Laboratory (MSL) mission is the first instrument to employ LIBS on another planet [3–5]. LIBS measurements are quick and only require optical access to the sample, allowing ChemCam to measure multiple samples each sol (i.e. each Mars-day), at distances of up to seven meters from the rover. Since the start of the mission in 2012, ChemCam has measured over 880,000 LIBS spectra on Mars [6] and has provided a detailed account of the changing composition of the Martian surface along Curiosity's traverse [7–11]. ChemCam's success has further increased the demand for LIBS on Mars, so that the two rover missions that landed on Mars in 2021 have both been equipped with LIBS instruments. NASA's Mars 2020 rover Perseverance is equipped with SuperCam [12,13], the enhanced successor of ChemCam, while the Zhurong rover of the China National Space Administration's (CNSA)

Tianwen-1 mission is equipped with the Mars Surface Composition Detector (MarSCoDe), a LIBS instrument suite inspired by ChemCam [14]. LIBS will therefore remain an important technique for Martian exploration in the coming years.

While LIBS measurements are straightforward, the data analysis can be challenging due to the complexity of the investigated laser-induced plasma [2,15,16]. Over the course of its lifetime, the plasma plume undergoes many stages, from its generation in the laser ablation process to the supersonic expansion following ablation and the eventual confinement by the ambient gas [17,18]. The transient and dynamic nature of the plasma means that the number densities of electrons, atoms, ions, and molecules in the plasma are heterogeneous and change over time. Likewise, temperature gradients in the plasma and the overall cooling of the plasma over time affect the emission and absorption coefficients of the plasma species. The plasma evolution and propagation are influenced by the initial ablation process and by the subsequent interaction with the environment. In the ablation process, chemical and physical properties of the sample and the parameters of the laser pulse determine the initial plasma formation and its composition. As the plasma propagates into the surrounding environment, the geometry of the sample surface and the pressure of the ambient gas strongly determine the evolution of the plasma plume by confining its expansion. The hot plasma also interacts with the sample surface and with the ambient gas, leading to further vaporization and ionization. Understanding these processes and their influence on the measured LIBS spectra is crucial in order to improve the accuracy of LIBS as an analytical technique. This is especially true for LIBS measurements of rocks and soils on Mars by ChemCam and its successors, since the measurement conditions vary significantly in dependence of the geological composition and surface geometry of the investigated targets at different distances from the rover [5,19].

A common approach to modeling the laser-induced plasma is to assume a uniform temperature and a homogeneous distribution of particles as well as the existence of local thermodynamic equilibrium (LTE) [20,21]. The plasma is then fully described by its temperature and electron density, the number densities of the atoms of each element, and the effective path length of emission and absorption. While this model can work reasonably well for strongly confined plasma plumes in high-pressure noble gas atmospheres, it usually fails to describe LIBS spectra sufficiently because of the inhomogeneous and transient nature of the plasma plume, which can result in spectral features of ions, atoms, and molecules that are only found at significantly different temperatures [22–24]. One frequently used modification of this model is therefore to describe the plasma plume as a two-layer system with a hot central layer and a colder peripheral layer, which may also have a different density [25,26]. This modification allows for the description of temperature-sensitive effects such as self-reversal of emission lines due to absorption in the cold periphery, or the simultaneous occurrence of molecules in the outer layer and ions in the inner layer. It has been shown that this model is able to describe measurements in air or in a noble gas atmosphere at pressures close to the standard atmospheric pressure of 101.3 kPa very well [25]. Recently, it has also been successfully applied to time-resolved LIBS spectra in Martian ambient conditions [27]. However, such a two-zone model does not agree well with hydrodynamic simulations of the plasma plume, which predict a more complex plasma with strong spatial variations of the emission due to temperature and pressure gradients [28] that often manifest as vortices inside the plasma plume [29]. Vortices and other turbulences have also been observed in shadowgrams of laser-induced plasmas [18].

In order to understand the distributions of excited species within the laser-induced plasma better and to investigate the influence of temperature and pressure gradients on these distributions, it is desirable to measure the emissions of these species with a dedicated plasma imaging setup that allows for spatially and temporally resolved measurements of the plasma emissions. This approach has already been successfully employed to laser-induced plasma plumes in air at standard atmospheric pressure or in a buffer gas like argon, showing significant differences in the distributions of different plasma species [e.g. 30–33]. On Mars, where the atmosphere consists mostly of CO_2 and has a low pressure between 700 Pa to 1000 Pa [34,35], spatial variations may be even more pronounced due to the lower confinement of the plasma plume as well as differences in the physical properties of CO_2 in comparison to air or argon affecting the plasma uniformity [36,37]. This could be relevant for the models that are used to analyze

the Martian LIBS spectra. One important example is the choice of a suitable normalization technique, which will strongly affect the results of both univariate and multivariate data analysis techniques, including the calibration models that are used to predict the chemical compositions of Martian rocks and soils investigated with LIBS [38]. Atmospheric emissions of C and O have been previously used as internal standards for normalization [39,40]. However, such a normalization will only be valid if the analyzed emission and the normalization emission originate from the same regions within the plasma plume. Plasma imaging measurements can also help to understand the relation between the LIBS spectrum and the acoustic signal of the laser-induced plasma, which is closely related to the plasma shock wave and has been of great interest due to the inclusion of a microphone in the SuperCam instrument suite [41,42].

In this study, we demonstrate the potential of plasma imaging measurements for the characterization of laser-induced plasma plumes in simulated Martian atmospheric conditions by investigating the spatial and temporal evolution of plasma emissions of a calcium sulfate sample in Mars-analogue gas at 700 Pa. Calcium sulfate veins frequently form in sedimentary rock and have been detected on Mars already in hydration states that suggest gypsum and basanite [43]. For this study, gypsum ($CaSO_4 \cdot 2H_2O$) is used, because it is a simple matrix with strong LIBS signals of Ca ions and atoms, of O and H atoms, and of CaO molecules that form in the plasma itself. Under the assumption of LTE, the distributions of emissions from Ca ions, Ca atoms, and CaO molecules are expected to correlate with different plasma temperatures. Meanwhile, the emissions of atomic O and H are expected to be more thermally stable, but could show a stronger influence of pressure gradients and flows within the plasma plume due to their lower mass. Furthermore, the simulated Martian atmosphere consisting mostly of CO_2 results in strong emissions of C ions and atoms and will also affect the O distribution in the plasma. The goal of the study is to investigate the relationship between plasma emissions and the kinetic and thermodynamic properties of the plasma plume in Martian atmospheric conditions more closely. The results are not only relevant for our understanding of Martian LIBS, but also to the LIBS technique in general.

2 Materials and methods

2.1 Samples

Measurements were made on samples made from pure, reagent-grade $CaSO_4 \cdot 2H_2O$ powder. The powder was pressed into round pellets of 13 mm diameter and about 2 mm height. A pressure of 370 MPa was applied for ten minutes to produce compact samples with a flat and smooth surface. A total number of three identically produced samples was used for this study in order to have enough surface area to make all measurements without repeatedly targeting the same position on the sample, which would disturb the smoothness of the sample surface and therefore affect the propagation of the plasma plume.

2.2 Time-resolved high-resolution LIBS setup

LIBS spectra in this study were recorded with the high-resolution LIBS system at the DLR Institute of Optical Sensor Systems in Berlin that was already described in previous publications (Schröder et al. 2013, Vogt et al. 2018, Schröder et al. 2019, Vogt et al. 2020, Hansen et al. 2021). Like the plasma imaging setup described in the next section, it features a low-pressure simulation chamber that was filled with a Mars-analogue gas mixture (95.55 vol% CO_2, 2.7 vol% N_2, 1.6 vol% Ar, and 0.15 vol% O_2) at a pressure of 700 Pa for all measurements to simulate Martian atmospheric conditions. The plasma is induced by a Q-switched Nd:YAG laser with a wavelength of 1064 nm, a pulse width of 6 ns (Continuum Inlite-II), and a pulse energy of 18 mJ. A high-resolution echelle spectrometer (LTB Aryelle Butterfly) records the LIBS spectra in one of two wavelength ranges, where the first covers the wavelengths from 190 nm to 375 nm and the second covers the wavelengths from 275 nm to 850 nm. The spectral resolution varies from 0.015 nm at 190 nm to 0.09 nm at 850 nm. The spectrometer is equipped with a time-gated intensified charge-coupled device (ICCD) camera (Andor iStar) that enables measurements at different delay times with a minimum gate width of 10 ns. The time-resolved LIBS measurements for this study were recorded with delay time steps of 200 ns, with a minimum delay time of 10 ns with respect to the laser incidence on the sample. The gate width for

the measurements was set to 100 ns and each recorded spectrum was averaged over 500 successive laser pulses on a moving sample in order to obtain a good signal-to-noise ratio.

2.3 Plasma imaging setup

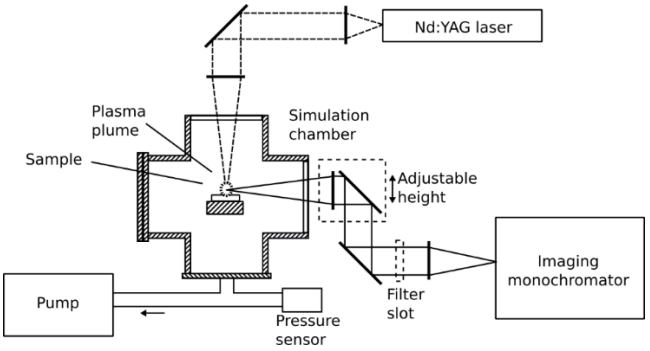

Figure 1: Schematic of the plasma imaging setup. Bandpass filters can be inserted in the filter slot shown in the optical path in front of the imaging monochromator.

The spatially and temporally resolved measurements in this study were made with a newly implemented plasma imaging setup at the DLR Institute of Optical Sensor Systems in Berlin, which is shown in Figure 1. The sample is placed inside a vacuum chamber, which is connected to a turbo pump and can be filled with the Mars-analogue gas mixture described in the previous section. The laser pulse of an actively Q-switched Nd:YAG laser (Quantel Viron, 1064 nm wavelength, 8 ns pulse width, up to 30 mJ/pulse) is guided vertically onto the sample surface in order to produce the plasma. The spot diameter in this study was measured to be approximately 150 µm. The plasma emission is detected through a window on the side of the vacuum chamber. The objective lens and the mirror behind it can be adjusted in height so that the plasma emissions can be measured at different heights. The emissions are focused onto the slit of the imaging monochromator (Andor Kymera 328i), which is equipped with an ICCD camera (Andor iStar) to enable time resolution in the nanosecond range. The ICCD is synchronized with the laser in order to start measurements at a precise time after the onset of the plasma. The monochromator is equipped with three gratings: UV (2400 l/mm, 240 nm blaze wavelength), VIS (1200 l/mm, 500 nm blaze wavelength), and NIR (1200 l/mm, 750 nm blaze wavelength). The width of the motorized slit of the monochromator can be varied from 10 µm to 2500 µm. The measurements in this study were all performed with the maximum slit width of 2500 µm in order to obtain images of the emission of the complete plasma plume in a single measurement. Spectral filtering was either achieved with a bandpass filter in the detection path, or by imaging the emission of an isolated spectral line so that the observed emission is not superimposed by other spectral features.

The plasma that is produced in the plasma imaging setup in simulated Martian atmospheric conditions is expected to be comparable to the plasma produced on Mars by instruments such as ChemCam or SuperCam on similar targets, for example on $CaSO_4$ veins in the case of the samples used in this study. The relevant measurement parameters that affect the spatiotemporal evolution of the plasma are the laser wavelength, the laser pulse duration, the laser irradiance on the sample surface, and the atmospheric pressure and composition. The laser wavelength is effectively the same as that of the LIBS instruments on Mars – the ChemCam Nd:KGW laser has a wavelength of 1067 nm, while both SuperCam and MarSCoDe also use a Nd:YAG laser at 1064 nm for LIBS [3,12,14]. The laser pulse durations of the three LIBS instruments on Mars are close to 4 ns, which is shorter than the 8 ns pulse duration of the laser in the plasma imaging setup. However, a significant impact of the pulse duration is only expected if the order of magnitude changes, for example if a picosecond laser is used [44]. The laser irradiance and the ambient conditions have been adjusted to be as close to the conditions on Mars as possible for this study.

2.4 Abel inversion

The spatially resolved measurements of the plasma imaging setup yield a side view of the plasma plume emissions, where for each point on the image the emissions are the result of cumulative emission and absorption along the line

of sight through the plasma plume. If the plasma is optically thin and symmetric about the central plasma axis, then absorption can be neglected and the measured intensity distribution for a specific spectral feature is given by

$$I(x) = 2\int_x^\infty \frac{r\,\varepsilon(r)}{\sqrt{r^2-x^2}}dr\,, \tag{1}$$

where x is the lateral position of the intensity profile, r is the radial position in the plasma, and $\varepsilon(r)$ is the radial emission coefficient of the transition in the plasma. The intensity distribution $I(x)$ is therefore the Abel transform of the emission coefficient $\varepsilon(r)$. To obtain $\varepsilon(r)$ from $I(x)$, an Abel inversion needs to be calculated. While this can be theoretically achieved by calculating the Hankel transform of the Fourier transform of $I(x)$, the inversion is very susceptible to experimental noise. Therefore, various numerical techniques for Abel inversions that are more robust with respect to noise have been proposed in the literature [e.g. 45–47]. One relatively simple and robust approach is to avoid a direct Abel inversion and instead to rely on fitting the Abel transform of an arbitrary distribution to the data. This is the approach that was used in this study. Since the measurement with the ICCD yields a discrete set I_k of intensity values with constant spacing Δx, the desired emission coefficient values are also discrete values ε_j with constant spacing $\Delta r = \Delta x$. The Abel transform can then be written as the matrix multiplication

$$A_{kj}\,\varepsilon_j = I_k, \tag{2}$$

with

$$A_{kj} = 2\left(\sqrt{(j+1)^2-k^2} - \sqrt{j^2-k^2}\right),\ k \le j, \tag{3}$$

which can be solved for ε_j via non-negative least-squares minimization. The advantage of this method is that the solution is guaranteed to be a *feasible* reconstruction of the emission coefficient, i.e. one that is physically possible and that accurately describes the observed data.

2.5 Plasma imaging measurements

For each investigated plasma emission, two series of 20 measurements each were obtained. In the first series, the ICCD delay with respect to the laser pulse was increased in steps of 10 ns, while the delay step in the second series was 100 ns. The gate width was set equal to the delay step for all measurements, so that the early plasma emissions have been recorded with a 10 ns gate width and the late plasma have been recorded with a 100 ns gate width. The delay between the laser pulse and the earliest ICCD delay setting used here was determined to be approximately 40 ns. Therefore, the measurements with 10 ns delay steps cover the early plasma evolution from 40 ns up to 250 ns after laser ablation, while the measurements with 100 ns delay steps cover the plasma evolution from 40 ns to 2040 ns. From here on, the delay times used for discussing the measurements will correspond to the time at the center of the integration window, since this allows for a more accurate comparison of the measurements with different gate widths.

Table 1: Emissions investigated in this study along with their emission wavelength and the method of measurement in the plasma imaging setup. (FWHM: full width at half maximum.)

Emission	Wavelength	Method of measurement
Ca II	373.7 nm	Isolated spectral line
Ca I	422.7 nm	Isolated spectral line
CaO (orange system)	~600 nm (multiple bands)	Bandpass (600 nm, 10 nm FWHM)
C I	247.9 nm	Isolated spectral line
C III	229.7 nm	Isolated spectral line
O I	777.4 nm	Bandpass (780 nm, 10 nm FWHM)
H I	656.3 nm	Bandpass (656.2 nm, 1.2 nm FWHM)
Electron continuum	(Continuous)	Emission from 320.8 nm to 322.1 nm

The investigated emissions are summarized in Table 1 together with the chosen measurement method, which is either to use a bandpass filter or to measure the spectrum of a signal that is sufficiently isolated for it to be imaged in two dimensions without significant superposition of other spectral features, as explained in section 2.3. The emissions were selected to represent features both from the ambient Mars-analogue gas, which mostly consists of CO_2, and from the sample itself. S could not be investigated, since it has only weak lines in the available UV/VIS/NIR spectral range that could not be detected with this experimental setup. The C I line at 247.9 nm and the C III line at 229.7 nm completely originate from the ambient CO_2, while the O I triplet at 777.4 nm is partially due to the ambient gas and partially due to the O in the $CaSO_4 \cdot 2H_2O$ samples. The H I line at 656.3 nm is the H_α line of the Balmer series, which is present due to the hydration state and because of water adsorption at the sample surface. In the case of C and Ca, the distributions of both atomic and ionic emissions were measured in order to observe the effect of changing temperature and electron density throughout the plasma plume. Furthermore, CaO molecules that form in the plasma plume are investigated via their orange system, which is a broad band system centering at around 600 nm. Under the assumption of local thermodynamic equilibrium (LTE), these CaO molecules are only present in significant concentrations at comparatively low temperatures. Lastly, the continuum in the spectrum is investigated as well because of its connection to the electron distribution in the plasma. No bandpass filter was available to measure the continuum without the interference of spectral lines, and it is not possible to obtain the two-dimensional spatial distribution of a continuous signal. Therefore, only the one-dimensional intensity distribution perpendicular to the plasma axis could be investigated and no Abel inversion could be calculated.

3 Results

3.1 High-resolution LIBS spectrum

Figure 2 shows the LIBS spectrum of $CaSO4 \cdot 2H_2O$ recorded with the high-resolution LIBS setup at a delay time of 150 ns and a gate width of 10 µs in the full wavelength range from 190 nm to 850 nm. The plasma emissions that are investigated with the plasma imaging setup in this study are marked with an asterisk. The spectrum is dominated by Ca II lines in the UV and Ca I lines in the visible range. H I, O I and atmospheric C I and C III lines as well as broad CaO band systems are observed as well. While S II lines are also present in the spectrum, they are too weak to be used in plasma imaging.

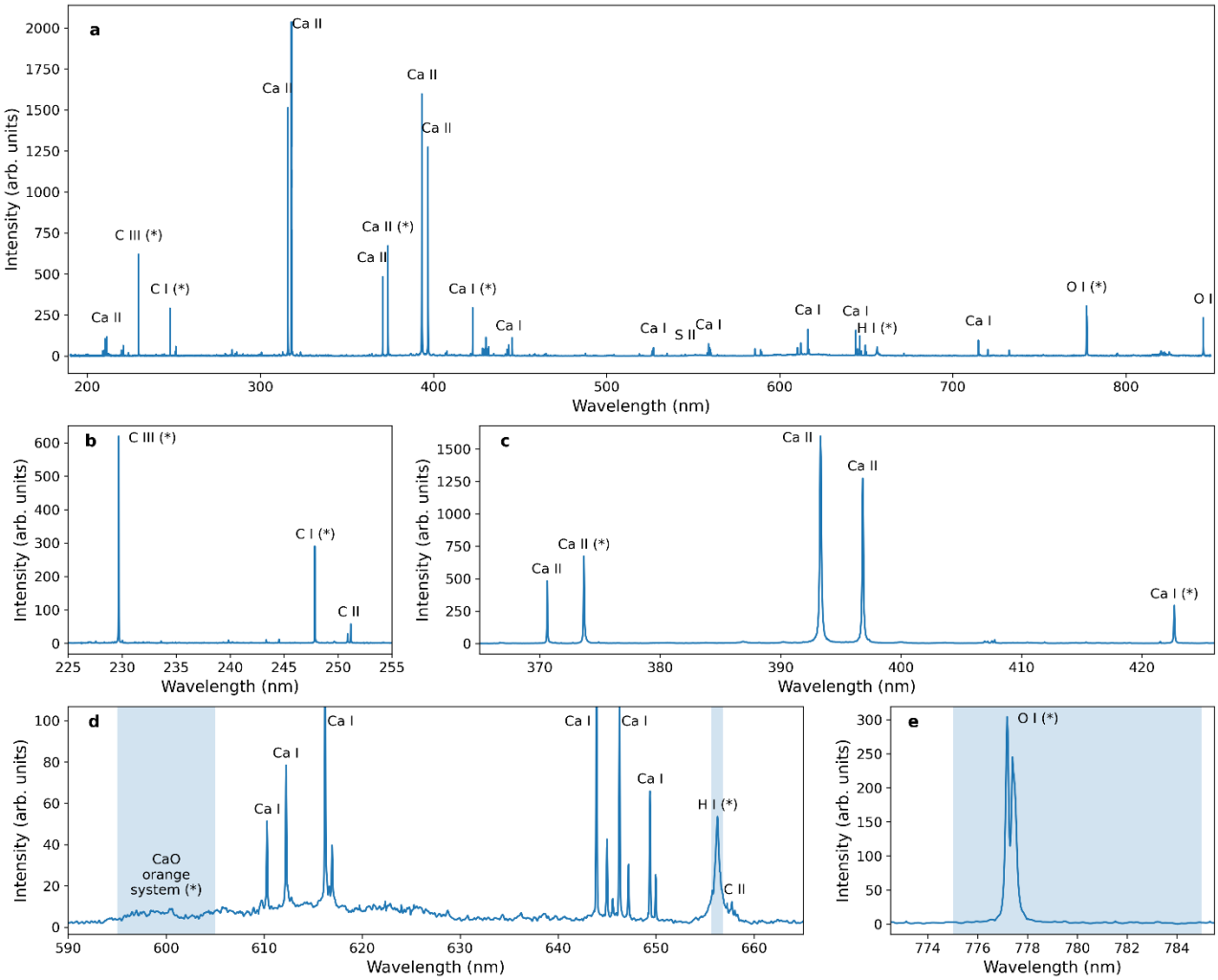

Figure 2: a) LIBS spectrum of $CaSO4 \cdot 2H_2O$ combined from both wavelength ranges of the high-resolution setup, measured in ambient Mars-simulant gas at a pressure of 700 Pa. Delay time and gate width are 150 ns and 10 µs, respectively. The emissions that are investigated in this study are marked with an asterisk. b) to e): Enhanced sections of the spectrum showing the investigated emissions. Filled areas show the wavelength ranges covered by the respective bandpass filters.

3.2 Time-resolved electron density and temperature

The electron density in the plasma can be calculated from the Stark broadening of the emission lines. The Stark broadening of the H I line at 656.3 nm is especially strong and has been investigated closely, so that the line is well-suited for the calculation of the electron density [48,49]. We use the compact formula first given by Gigosos et al. [50], which has since been corrected [51,52] to relate the electron density to the full width at half maximum (FWHM) so that

$$\mathrm{FWHM} = 1.098\ \mathrm{nm} \times \left(\frac{N_e}{10^{23}\ \mathrm{m^{-3}}}\right)^{0.67965},$$

where N_e is the electron density. Figure 3a shows the Lorentzian fit of the H I line for the time-resolved LIBS spectrum recorded with a delay time of 410 ns. Calculating the electron density for all time-resolved LIBS spectra this way, we obtain the electron density in dependence of the delay time, see Figure 3b. The decrease of the electron density in dependence of the delay time t_D is fitted with the exponential decay function

$$N_e(t_D) = (1.0 \pm 0.2) \times 10^{23}\ \mathrm{m^{-3}} \times e^{-(4.1 \pm 0.8)\ \mu\mathrm{s}^{-1}\, t_D} + (1.4 \pm 0.6) \times 10^{22}\ \mathrm{m^{-3}} \times e^{-(0.4 \pm 0.3)\ \mu\mathrm{s}^{-1}\, t_D}.$$

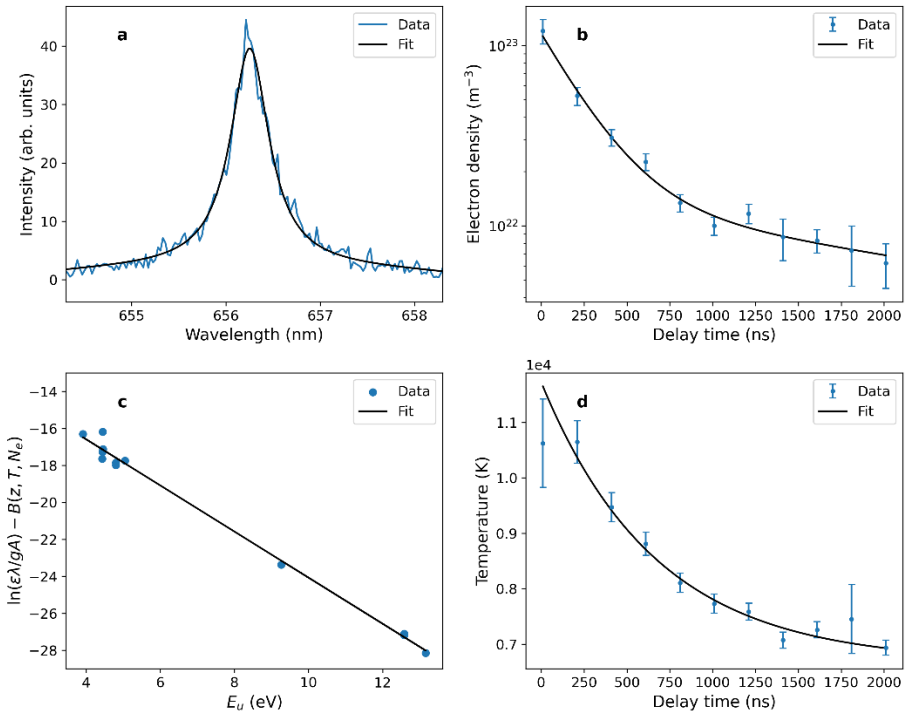

Figure 3: a) H I line at 656.3 nm and its Lorentzian fit in the time-resolved LIBS spectrum of $CaSO_4 \cdot 2H_2O$ recorded with a delay time of 410 ns and a gate of 100 ns. b) Electron density values calculated from the H I line fits in dependence of the delay time, fitted with the sum of two exponential decay functions. c) Saha-Boltzmann plot made with selected Ca I and Ca II lines from the time-resolved LIBS spectrum recorded with a delay of 410 ns and fitted with a linear regression to obtain the temperature from the slope. d) Temperature values calculated from Saha-Boltzmann plots in dependence of the delay time, fitted with an exponential decay with an offset.

The temperature of the laser-induced plasma can be calculated from Saha-Boltzmann plots under the assumption that the plasma is in LTE, optically thin and isothermal [53,54]. The Saha-Boltzmann plot is based on the following equation, which relates the emission coefficient ε_{ul} of a spectral line of a plasma species to the upper energy level E_u^* of the transition:

$$\ln\left(\frac{\varepsilon_{ul}\lambda_{ul}}{A_{ul}g_u}\right) - B(z,T,N_e) = -\frac{E_u^*}{k_B T} + \ln\left(\frac{hcN_0}{Q_0(T)}\right)$$

Here z is the ionization of the species, λ_{ul} is the wavelength of the spectral line, A_{ul} is the transition probability, g_u is the degeneracy of the upper energy level, k_B is the Boltzmann constant, T is the temperature, h is the Planck constant, c is the speed of light, N_0 is the number density of the atomic species, and $Q_0(T)$ is the partition function of the atomic species. The upper energy level E_u^* is relative to the ground state of the atomic species, so that it must be corrected for ionic species by adding the sum of all lower ionization energies required to produce this ionic species. Furthermore,

$$B(z,T,N_e) = z\ln\left[\frac{2}{h^3}(2\pi m_e k_B)^{\frac{3}{2}}\frac{T^{\frac{3}{2}}}{N_e}\right]$$

is a correction term that depends on the ionization, the temperature, and the electron density N_e, with m_e being the electron mass. The Saha-Boltzmann plot is constructed by plotting E_u^* on the x-axis and the left term of the Saha-Boltzmann equation on the y-axis, which yields a linear trend with a slope of $-(k_B T)^{-1}$. Since $B(z,T,N_e)$ depends on the temperature, the Saha-Boltzmann plot needs to be solved iteratively.

The spectral lines that were used for the temperature calculation and the corresponding parameters are summarized in Table 2. Figure 3c shows a typical Saha-Boltzmann plot along with the linear fit that is used to calculate the temperature. The calculated temperature values in dependence of the delay time t_D are shown in Figure 3d. Here, an exponential decay function with an offset was used to fit the data, yielding the fit function

$$T(t_D) = (5000 \pm 400)\ \mathrm{K} \times e^{-(1.5\pm0.2)\ \mu\mathrm{s}^{-1}\, t_D} + (6700 \pm 200)\ \mathrm{K}.$$

Based on this fit, the temperature decreases from an initial value of about 11700 K to a value of about 6700 K within the investigated timespan.

Table 2: Spectral lines used for the Saha-Boltzmann temperature calculation from the time-resolved LIBS spectra. The line parameters are taken from the NIST spectral lines database [55].

Species	λ (nm)	g_u	A_{ul} (s^{-1})	E_u^* (eV)
Ca I	430.774	1	2.0×10^8	4.7631683
Ca I	431.865	3	7.4×10^7	4.7690284
Ca I	585.745	5	6.6×10^7	5.0486176
Ca I	616.217	3	4.8×10^7	3.9103990
Ca I	643.907	9	5.3×10^7	4.4506470
Ca I	644.981	5	9.0×10^6	4.4430250
Ca I	646.257	7	4.7×10^7	4.4409544
Ca I	649.378	5	4.4×10^7	4.4300117
Ca II	315.887	4	3.1×10^8	13.160329
Ca II	370.603	2	8.8×10^7	12.581035
Ca II	373.690	2	1.7×10^8	12.581035
Ca II	849.802	4	1.1×10^6	9.2641440

3.3 Measured plasma images

Figure 4 shows the plasma imaging measurements of Ca II, Ca I, CaO, C I, O I, and H I prior to Abel inversion for various delay times, measured with a 100 ns gate width and normalized to the maximum intensity for each delay time. Due to the normalization, intensity changes over time cannot be observed in these images. The C III emissions are omitted here, since they were only observed in the early plasma. For signals that were not measured with a bandpass filter (Ca II, Ca I, and C I), the superimposed continuum can be observed in the 190 ns delay time measurements as a vertical band around the plasma axis. The Ca I measurement at 190 ns delay additionally showed emissions from several superimposed emission lines of O II and Ca I at wavelengths between 428 nm and 432 nm, which have been removed for this figure. The observed signal at 190 ns delay in Figure 4c is likely also not representative of the CaO emission, since CaO is expected to form later in the plasma. It is more likely that it is actually the emission of the continuum in the range of the 600 nm bandpass filter that was used to capture the CaO signal, since it is only present at this earliest delay time.

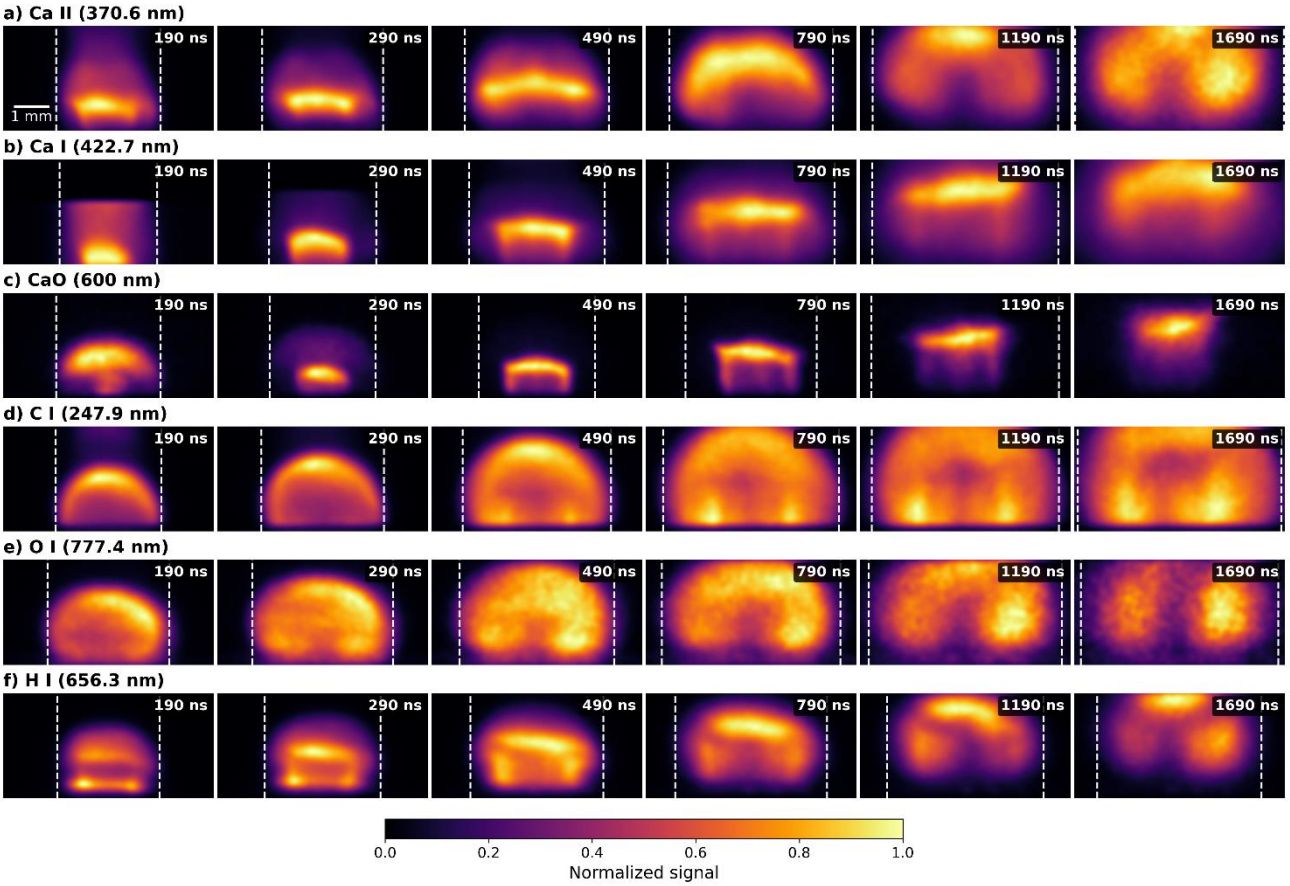

Figure 4: Examples of the recorded emissions for the investigated spectral features at different delay times and with a gate width of 100 ns. Lighter colors indicate stronger emission from this spatial region. The dashed lines mark the horizontal extents of the emissions.

The observed distributions of the plasma emissions all look different. At 490 ns delay, the ionic Ca II emission develops a horizontal high-intensity band at a medium height of 0.9–1.5 mm above the sample, while the atomic Ca I emission and the molecular CaO emission have similar, but smaller bands at lower heights (approximately 0.7–1.4 mm for Ca I and 0.7–1.2 mm for CaO). The atomic C I and O I emissions are both nearly hemispherical, but the C I emission is most intense in the outer regions of the plasma while the O I emission seems to be more evenly distributed within the plasma. The H I emission develops distinct regions at the top of the plasma and on the sides. The differences in the distributions indicate gradients of the element concentrations, but also of the temperature and the electron density within the plasma.

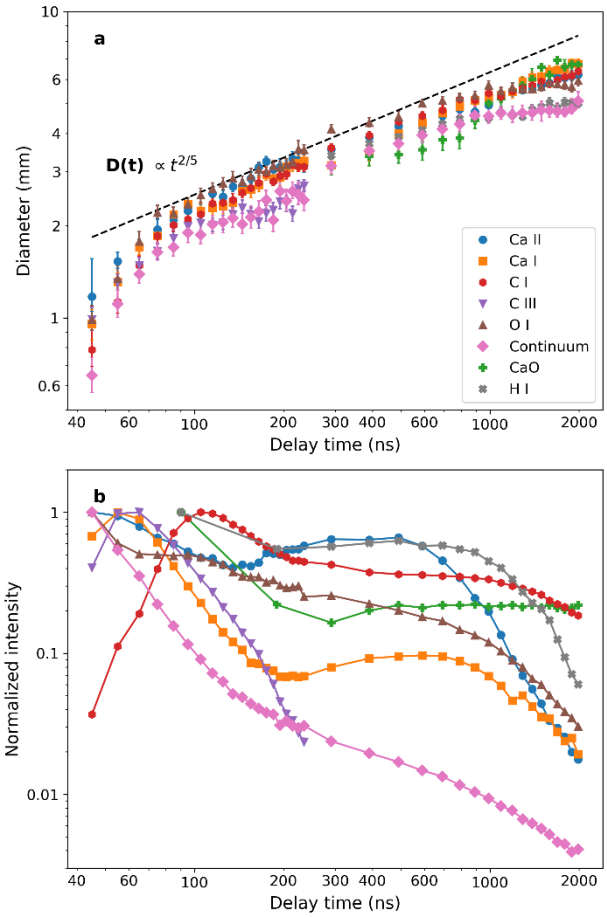

Figure 5: a) Diameters of the plasma emissions in dependence of the delay time. The diameters in the early plasma are well-aligned with the expected trend of the diameter of an expanding shock wave, which theoretically is given by $D(t) \propto {t_D}^{2/5}$. Their expansion starts to slow down at a delay of about 500 ns. b) Total intensities of the plasma emissions in dependence of the delay time, normalized to the maximum intensity of each emission. For emissions that have been measured with the shorter and the longer gate width, the influence of the gate width on the intensity has been corrected by dividing the shorter-gate signal intensities by the ratio to the longer-gate signal intensities of the respective emission in the time region where both series overlap.

Despite the differences in the signal distributions, the outermost extent of most distributions is similar and most emissions have a nearly hemispherical shape at the plasma periphery. In order to quantify this observation for all delay times, the extent of all distributions was measured and is indicated in Figure 4 by the dashed lines showing the left and right boundaries of the emissions. The boundaries were determined by finding the positions where the signal intensities were 20% of the local maximum intensity near the boundary. Figure 5 shows the determined signal diameters and their confidence intervals in dependence of the time. The black dashed line represents the theoretical time evolution of the shock wave diameter given by the Taylor-Sedov model, which is given by $D(t) \propto {t_D}^{2/5}$ [18]. The emission diameters do not follow this trend in the very early plasma, but follow it closely from a delay of about 80 ns to 500 ns. After 500 ns, the emissions slow down relative to the shock wave model, which is also the time where the decoupling of the shock wave has been observed previously [18].

The C III and continuum emissions are confined to a smaller region around the plasma center from the start, indicating that the temperature decreases from the plasma center to the outer plasma in the early stages of the plasma expansion. However, it can also be observed that the CaO emission is confined to a small diameter at a delay of about 500 ns, which suggests that the temperature in the plasma center decreases significantly as the plasma expands. As the plasma cools down over time, the CaO emission is also seen to reach further out until its diameter is similar to that of C I, O I, Ca II, and Ca I. The continuum emission and the H I emission remain confined to a smaller plasma region at all delay times.

While the previous considerations are independent of the intensity, it is also worth investigating how the intensities of the signals change over time. This is shown in Figure 5b for the normalized total intensity of each signal over time. In order to obtain intensity curves that are not distorted by the change in the gate width between the different measurement series, the signal intensities from measurements with the shorter gate width were divided by the ratio to the signal intensities from measurements with the longer gate within the time region where both series overlap. As expected, the general trend is that the intensities decrease over time as the plasma expands and its temperature decreases, which is especially noticeable in the strong decrease of the continuum signal and the C III signal in the early plasma and the strong decrease of the Ca II and H I signals in the late plasma. However, the signals can also be seen to increase at certain delay times. C III and Ca I increase between 45 ns and 55 ns delay, while C I strongly increases up to a delay of 115 ns. The Ca I signal likely shows this initial decrease because of plasma cooling and recombination of Ca ions to atoms. For the C signals, the initial increase could also be related to the ongoing vaporization of the ambient CO_2 gas, which will generate a higher number of C atoms and ions. This effect cannot be observed for O I, but this is expected because there is already a significant amount of O in the sample, and the early measurements of O I are also superimposed by continuum emission. Ca I, Ca II and H I also show an increasing trend between approximately 200 ns and 600 ns delay, potentially indicating a brief reheating of the plasma. An exception to the general decline of the intensity is the CaO signal, which falls quickly in the first 200 ns but then increases slowly for the later delay times. The initial decay of the CaO signal has a very similar rate as the decay of the continuum, which indicates that these first 200 ns are indeed dominated by continuum emission within the wavelength range of the bandpass used to measure CaO. CaO molecules only form once the temperature has cooled enough, indicating that at approximately 300 ns delay there is already a low-temperature region in the plasma even though the Ca II emission is still very high at this point. As the plasma cools over time, the conditions within the plasma become even more preferable for CaO formation and more CaO emission can be observed.

3.4 Radial distributions of emissions

In order to analyze the radial distributions of the emissions, the Abel inversion was applied to the spatially resolved measurements. Figure 6 shows the results for the emissions of Ca II, Ca I, CaO, C I, O I, and H I measured with a gate width of 100 ns at the delay times of 190 ns, 290 ns, 490 ns, 790 ns, 1190 ns, and 1690 ns. Figures showing the radial distributions at all investigated delay times for each emission are found in the supplementary material for this article. Each image in Figure 6 is normalized to its maximum intensity to provide visual clarity. However, this means that intensity changes over time cannot be observed in these images.

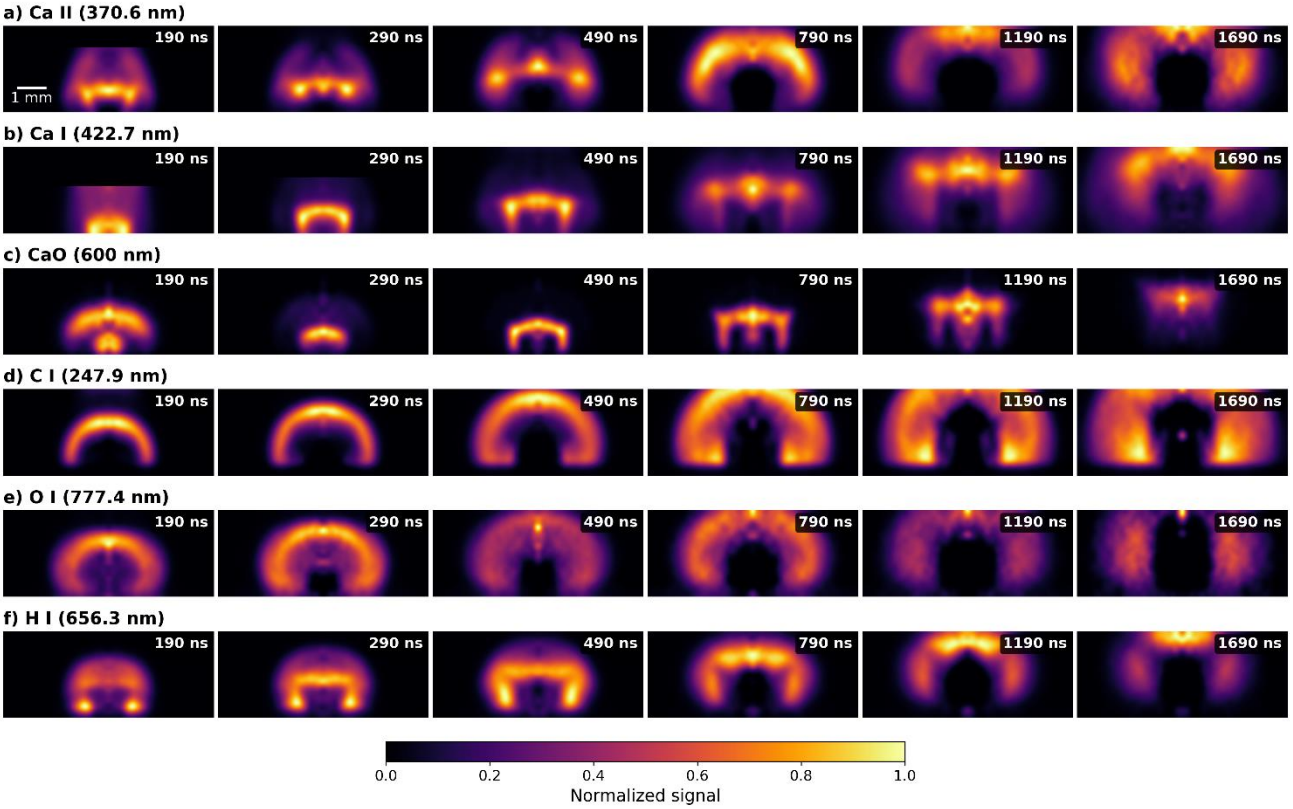

Figure 6: Radial distributions of the investigated emissions at various delay times obtained by Abel inversion. The calculated radial emissions have been mirrored along the plasma axis. Lighter colors indicate stronger emission. Figures showing the results for all delay times for each emission can be found in the supplementary material for this article.

In the case of the Ca emissions, it can be seen that the spatial distributions are quite different. Ca II generally emits more strongly in the outer parts of the plasma, while Ca I and CaO emit closer to the plasma axis. From 490 ns on, there is a clear lack of Ca II emission in a spherical volume close to the sample surface around the plasma axis. The same region still features low emission from Ca I and moderate emission from CaO. This indicates that this region is a rarefied low-temperature region where the general concentration of Ca ions and atoms is low and the lower temperature is favorable for the formation of CaO molecules. Directly above this rarefaction zone, stronger emissions from all three signals can be observed, indicating a higher plasma density as well as a higher temperature. The strong spatial variation of these Ca and CaO emissions shows that the plasma properties vary on a highly localized level.

The radial distributions of C I and O I are very similar and resemble the dome-like density distribution of the outgoing shock wave. The main difference is that the C I distribution shows a sharp contrast between regions of high emissivity and adjacent regions of low emissivity, while the O I emissivity declines more gradually from its regions of highest emissivity. This could be related to the fact that the only source for C is the ambient CO_2 gas, whereas large amounts of O will also be released during the ablation of the $CaSO_4 \cdot 2H_2O$ sample itself. Furthermore, atomic C forms in a narrower temperature range than atomic O: its concentration at high temperatures is more limited due to its lower ionization energy (11.26 eV for C versus 13.62 eV for O), while its concentration at lower temperatures is also more limited due to the presence of CO, which has a higher dissociation energy than O_2 (11.2 eV for CO versus 5.2 eV for O_2 [56]) and takes up one C and one O atom from the original ambient CO_2, leaving a surplus of O atoms at low temperatures. It is therefore likely that these temperature-related concentration changes play a significant role in the appearance of these distributions. Unfortunately, neither strong emissions of C II and O II nor molecular emissions of CO could be observed in the available wavelength range of the experimental setup, so that a closer investigation of this effect was not possible.

The H emission is slightly more confined than the C and O emission, but is also low at the plasma center itself. A horizontal region of high emissivity can be seen above the rarefied plasma center, which is similar to the feature observed in the Ca II and Ca I emissions. Close to the sample surface at a radius of about 1 mm, local high emission coefficients can be observed in the measurements at lower delay times up to 490 ns, which could indicate the presence of vortices in these regions close to the sample surface where the local number densities of the atoms are increased.

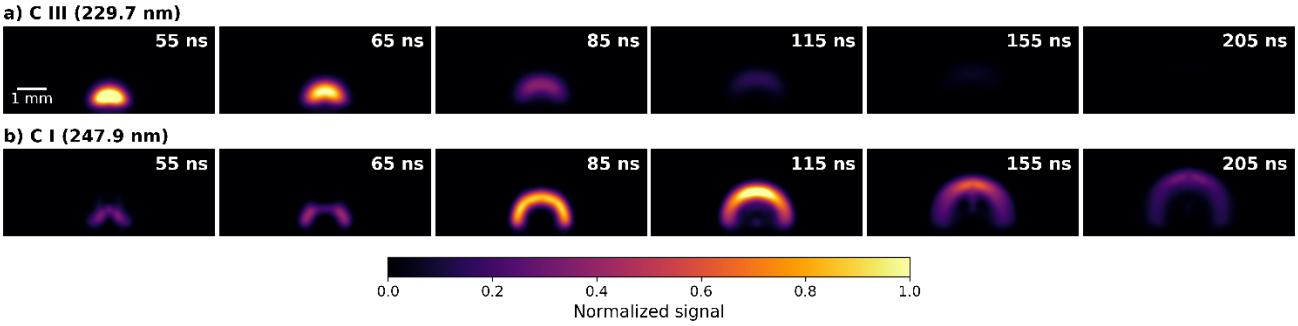

Figure 7: Radial distributions of a) C III and b) C I at different delay times. The distributions have been mirrored along the plasma axis. Lighter colors indicate stronger emission. Each signal was normalized to the maximum intensity of the respective time series and the color scale was capped at 70% of the maximum intensity in order to improve visual clarity.

The comparison of the spatially resolved emissions of C I and C III in the early plasma is of special interest, since it offers insight into the early plasma evolution. In Figure 7, the two radial distributions are shown at delay times of 55 ns, 65 ns, 85 ns, 115 ns, 155 ns, and 205 ns. In this case, all images of the C III time series were normalized to the same maximum value and all images of the C I time series were normalized to the same maximum value, respectively. This makes it possible to see the intensity change over time, where the C III emission is most intense at the earliest delay times and then quickly decreases in intensity, while the intensity of the C I is initially low and increases until it reaches its peak at 115 ns and then decreases again. Furthermore, the two emissions are mostly located in different plasma regions, with the C III emission located directly in the center of the plasma and the C I emission located in a dome-like distribution around the C III emission. The presence of the C III emission in the center of the plasma indicates that the plasma center at early times is hot and rarefied, since high temperatures and low electron densities are favorable for ionization according to the Saha equation. The higher electron densities closer to the outgoing shock wave instead favor recombination to atomic C.

3.5 Temperature distribution in the plasma

Under the assumption of LTE and an optically thin plasma, the temperature distribution within the plasma plume can be calculated from local Saha-Boltzmann plots using the spatially resolved emissions [30]. Since we used a bandpass filter to measure the spatial distribution of the H I, it was not possible to obtain the electron density from the H I line width in the spatially resolved measurements. Therefore, the fit from the time-resolved LIBS spectra, see Figure 3b, was used to approximate the electron density for the spatially resolved measurements.

Table 3: Spectral lines used for the Saha-Boltzmann temperature calculation in the spatially resolved measurements. The line parameters are taken from the NIST spectral lines database [55].

Species	λ (nm)	g_u	A_{ul} (s^{-1})	E_u^* (eV)
C III	229.687	5	1.376×10^8	53.729955
C I	247.85612	3	2.8×10^7	7.68476777
Ca II	370.6024	2	8.8×10^7	12.581075
Ca I	422.673	3	2.18×10^8	2.9325120

Table 3 shows the emissions that were used for the temperature calculations in the plasma imaging measurements. The temperatures for the early plasma are calculated from the C I and C III lines, while the temperatures for the late

plasma are calculated from the Ca I and Ca II lines. It is important to note that the investigated Ca I line is usually strongly self-absorbed, which is not ideal for the temperature calculation. However, it is assumed here that the impact on the temperature is not strong since it appears in the logarithm of the Saha-Boltzmann calculation. Based on their spatial distributions, the two Ca emissions are the most suitable emissions for the temperature calculation, since they have a large spatial overlap and emit strongly at nearly all delay times. However, their signals are superimposed by the electron continuum in the early plasma, making it difficult to separate between the Ca emissions and the continuum. Therefore, the C lines were used to calculate the temperature distribution in the early plasma.

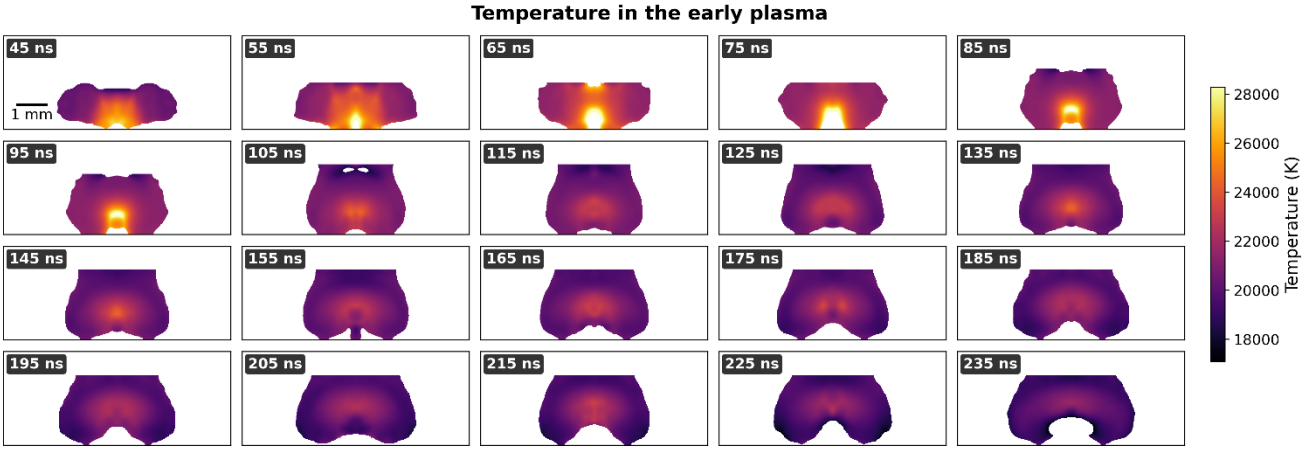

Figure 8: Spatial temperature distribution calculated from the C III and C I emissions for the early delay times. The temperature distribution has been mirrored along the plasma axis. White indicates regions where no temperature could be calculated due to the lack of at least one of the two signals.

The temperature distributions in the early plasma calculated from the C III and C I emissions are shown in Figure 8. Since the emissions do not overlap strongly, the plasma regions for which temperatures could be calculated are limited and the temperature at the plasma center around could sometimes not be calculated. However, the calculated temperature distributions indicate that the plasma center in the early plasma is hotter than the plasma periphery. The absolute temperature values are significantly higher than the ones calculated from the Ca lines in the 1D LIBS spectra in Figure 3d, which could indicate that the electron density values obtained from Figure 3b may not be valid for the early plasma and for the regions where the two C emissions overlap, which is mostly in the plasma center where no H emission could be observed (see Figure 6). Since this region in the plasma center is likely rarefied in comparison to the region of high H emission from which the electron density was obtained, the actual electron density may be significantly lower, which would lower the calculated temperature values and would also correspond well with a higher degree of ionization in this region.

The temperature distributions at later delay times calculated from the Ca emissions are shown in Figure 9. The temperature calculation was only done for those plasma regions where both the Ca II and the Ca I emission were clearly above the noise threshold, so that no temperatures are available for the shortest delay time of 90 ns, for the plasma periphery, and for the plasma center at later delay times. Furthermore, in the measurements at early delay times (up to 390 ns), parts of the measurement were manually removed from the temperature calculation due to overlaps with ionic signals in the Ca I measurements. Some artefacts from such overlaps can still be seen in the temperature distributions.

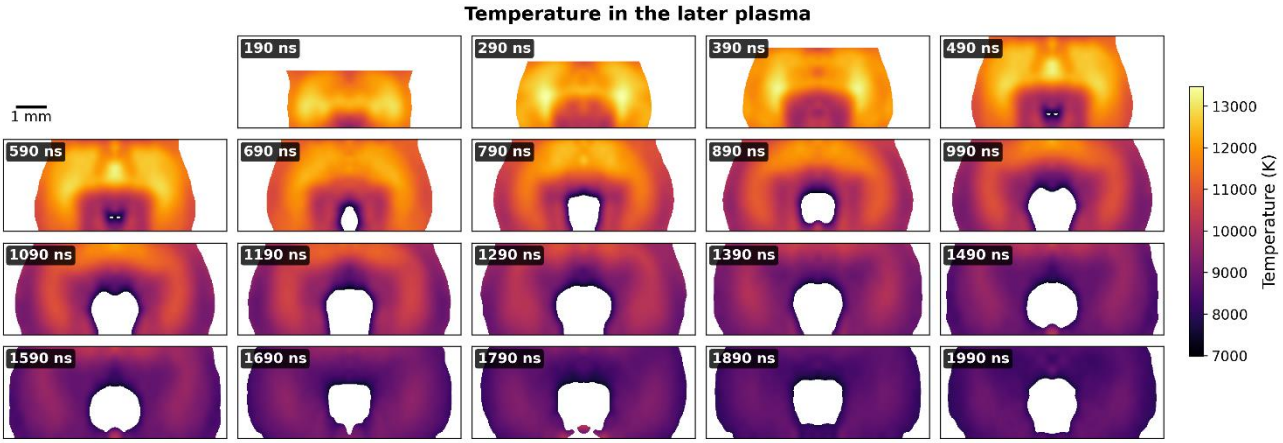

Figure 9: Spatial temperature distribution calculated from the Ca II and Ca I emissions for the later delay times. The temperature distribution has been mirrored along the plasma axis. White indicates regions where no temperature could be calculated due to the lack of at least one of the two signals.

The temperature distributions at the later delay times yield some important information about the plasma evolution. One observation is that there is a consistent low-temperature region at the plasma center. While direct temperature values of the plasma center are missing for most delay times, there is a clear trend of decreasing temperatures towards the center, with the calculated temperatures closest to the plasma center generally being below 8000 K. This is in line with the observations of the radial distributions of various emissions, specifically with that of the molecular CaO emission that is most intense close to the plasma center. Furthermore, the strong temperature gradients observed especially at earlier delay times of up to 1 µs explain the simultaneous presence of ionic, atomic and molecular emissions even at early times of the plasma evolution. Over time, these temperature gradients gradually decrease and homogenize as the plasma cools, so that the plasma is nearly isothermal at later delay times.

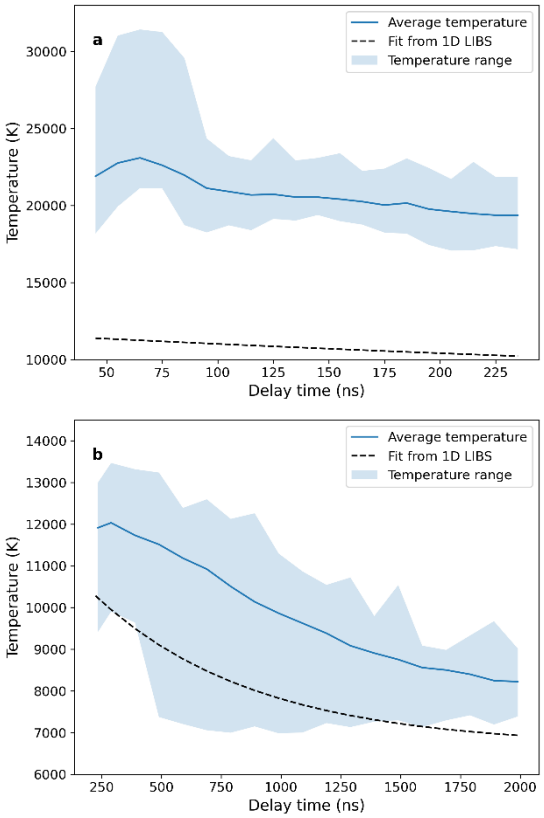

Figure 10: Comparison between the temperatures calculated from the spatially resolved measurements and from the 1D LIBS measurements in section 3.2. The light blue area marks the observed temperature range in the spatially resolved measurements, the blue solid line marks the average temperature calculated from all observed temperature values for a given delay time, and the black dashed line is the temperature fit obtained for the time-resolved LIBS measurements, see also Figure 3d. a) Values for the early plasma obtained using C III and C I. b) Values for the late plasma obtained using Ca II and Ca I.

Figure 10 summarizes the temperature distributions calculated from the spatially resolved measurements. The light blue area indicates the range of observed temperatures for a given delay time, while the dark blue line indicates the average temperature calculated from all observed temperatures in the plasma at a given delay time. The black dashed line shows the temperature fit from the LIBS measurements in section 3.2, see Figure 3d. In Figure 10a, the results for the temperatures calculated from the C emissions in the early plasma are shown. The maximum temperature at early delay times is significantly higher than the average and the minimum temperatures due to the small size of the high-temperature region at the plasma center. The temperature fit from the 1D LIBS measurements does not correspond well to the temperatures calculated from the C lines. As stated above, this is likely because the electron density used for the temperature calculation does not accurately represent the overlap region of the C I and C III emissions near the plasma center, where no hydrogen emission is observed. In Figure 10b, the temperatures obtained from the Ca emissions are better aligned with the same temperature fit, but the fit is still significantly lower than the average temperature. For a higher accuracy of the temperature calculations, a spatially resolved electron density measurement is therefore necessary. Still, the spatially resolved temperatures obtained here can be analyzed qualitatively. It can be seen that the range of temperatures is especially large around a delay of 500 ns, after which it decreases as the plasma cools and becomes more homogeneous. The earlier delay times are therefore not well-represented by a single temperature value such as that obtained from Saha-Boltzmann plots of spatially integrated LIBS measurements. Especially the minimum temperature is much lower than the average temperature, allowing for the formation of CaO molecules at earlier times than the average temperature would suggest. The minimum temperature seen here stays close to 7000 K after the initial drop at around 500 ns, which is likely the threshold above which Ca atoms and ions are present in sufficient amount to enable the temperature calculation via their emissions. The plasma center, where the CaO emission is most intense, might therefore be even colder.

4 Discussion

The strong spatial variations of the plasma emissions suggest a significant influence of temperature gradients and pressure gradients within the plasma. The observed distributions of the laser-induced plasma in Martian atmospheric conditions look very reminiscent to those predicted by numerical simulations of the laser-induced plasma [29], with strong emissions close to the shock front, rarefaction in the center, and apparent vortices and turbulences above the sample surface. While the individual distributions of the different species vary significantly from one another, the diameters of most emissions are approximately similar in diameter, though the atmospheric emissions tend to have a slightly wider diameter and the continuum and H I emissions have slightly smaller diameters. Their propagation follows the Taylor-Sedov model between 80 ns to 500 ns after the laser pulse, but slows down at later times, indicating the onset of atmospheric confinement and the decoupling of the shock wave. At least two distinct phases of the plasma propagation can therefore be observed in the spatial distributions of the emissions: the early plasma before 500 ns, which is coupled to the outgoing shock wave and is defined by the shock wave dynamics and corresponding strong internal density and temperature gradients, and the late plasma after 500 ns, which is more stationary and is defined by homogenization processes as the plasma cools and plasma species that were previously confined to small regions within the plasma start to diffuse. The homogenization in the late plasma can also be observed in the temperature distribution, which initially shows strong gradients within the plasma that start to decrease as the influence of the shock wave dynamics tapers off. The very early plasma before 80 ns could be another distinct phase in which the plasma plume size is still close enough to the initial explosion size that the Taylor-Sedov model's assumption of large distances is not yet valid. This very early plasma has a high degree of ionization and strong continuum emission, indicating high temperatures at the plasma center. However, it is not clear whether LTE is a valid assumption for this very early stage of the plasma.

The molecular CaO band emits most strongly in the plasma center, while the atomic and ionic Ca emissions originate mostly in the outer plasma closer to the plasma front and do not emit from the plasma center. Since CaO molecules are stable at lower temperatures than Ca atoms and ions, this means that the plasma center is significantly colder, which is further confirmed by the spatially resolved temperature calculations in Figure 9 that show a decreasing temperature towards the plasma center. The lowest calculated temperature values stay close to 7000 K from 500 ns on (see Figure 10b), but the temperature at the center is likely even lower, since the calculated temperatures are only valid for regions where atomic and ionic emissions are already present. The strong temperature gradients within the plasma explain why intense ionic, atomic, and molecular emissions can be observed at the same time and why CaO emission can be observed even at early delay times of about 300 ns, where temperature calculations from spatially integrated LIBS spectra yield temperature values that would otherwise be too high for a significant CaO concentration. Since all of the other emissions that were investigated at the later delay times show a striking lack of emission from the center, it can be concluded that the low-temperature zone there is linked to a strong rarefaction in the wake of the outgoing shock wave. These temperature and density gradients indicate that a full description of the plasma would require complex hydrodynamic simulations that consider the temporal evolution of the temperature, pressure and density gradients within the plasma. Indeed, reported results of hydrodynamic simulations of the plasma are qualitatively very similar to the spatial distributions and temperature gradients that are observed in this study, although they do not predict a cold plasma core in which molecules can form [28,29]. This difference could be explained by the choice of simulation parameters in the simulations, which represent non-Martian atmospheric conditions and in [29] also include a melting sample surface that reheats the plasma. For spectral analysis via calibration-free LIBS, simplified one-zone or two-zone models are preferred over computationally expensive hydrodynamic simulations and have been successfully applied to LIBS spectra obtained in Martian conditions [27]. Two-zone models generally find a hot inner zone and a colder outer zone in which self-absorption occurs [25,27]. The results from this study indicate that these two zones represent regions close to the plasma front, while the internal structure of the plasma can be more complex. This suggests that the innermost colder part of the plasma does not affect the LIBS spectrum strongly, with the notable exception of the presence of molecular bands in LIBS spectra. Since no molecular emission was observed in the regions near the plasma front,

our results indicate that molecular bands only appear in the spectra because molecules can form in the low-temperature plasma center.

Previous studies performed in air or in argon atmosphere have reported that spectral features of the atmospheric contributions were observed closer to the plasma periphery than other signals [30,31]. This observation is also true for the C I emission in our study. However, the C III emission in the early plasma is found directly in the center of the plasma, with the C I emission distributed in a layer around it. Therefore, the apparent concentration of C I in the plasma periphery could also be explained by temperature gradients within the plasma and by the differences in the ionization energies, which lead to differences in the relative concentrations of the ionization states for different elements. The strong C III emission in the center of the early plasma, which also does not move outwards appreciably over time, certainly suggests that a high concentration of C ions is generated during or immediately after the ablation process, so that the results do not support a model in which atmospheric emissions should only be found in the plasma periphery. However, even if C atoms and ions are distributed more evenly in the plasma than it appears from the C I emission alone, the differences in the spatial distributions of the C I emission and the sample-related emissions indicate that the C I emission is not ideal for the normalization of other spectral line intensities, because the plasma parameters that determine the C I emission in the outer plasma do not accurately reflect the plasma parameters that determine the emissions of spectral features that originate from the inner plasma regions [cf. 40]. The O I emission, which is partially due to atmospheric O and partially due to O in the sample, may be a better candidate for such normalization methods, since it was observed to be more homogeneously distributed within the plasma plume.

The temperature distributions that have been calculated from C and Ca emissions indicate a reversal, where the early plasma features high temperatures in the plasma center while the plasma later has a very low temperature at the center and higher temperatures in the outer regions. This may be explained by a smaller plasma volume in the early plasma, where most of the plasma center is still close enough to the shock wave to experience high temperatures. The quickly expanding plasma plume then experiences rarefaction and corresponding cooling at the plasma center, while the plasma front retains a high density and a high temperature. The strong C III emission close to the plasma center in the early plasma also suggests a significantly lower electron density that allows for a higher degree of ionization. Such a local variation of the electron density would also explain why the temperatures calculated from the C emissions are higher than the ones calculated from the Ca emissions, since the electron density used in the temperature calculations was calculated from the spatially integrated hydrogen line width that better represents the plasma regions with high Ca emissions.

5 Conclusion

In this study, we show first results from our plasma imaging setup, which allows for a spatial and temporal characterization of the plasma emissions in simulated Martian ambient conditions. Investigating the spatiotemporal evolution of the plasma plume in Mars-like atmospheric conditions allows us to better understand the plasma properties and processes that influence LIBS spectra recorded by instruments such as ChemCam and SuperCam on Mars. The results show complex spatial distributions of the atoms, ions and molecules in the plasma, which are strongly affected by local temperature and density gradients within the plasma plume. These local variations are likely the result of dynamic processes in the quickly expanding plasma plume, as indicated by features that resemble vortices and reflected shock waves. This suggests that the laser-induced plasma on Mars is heterogeneous and is not fully described by plasma models that assume an isothermal and homogeneous plasma. This assumption is implicit in many common methods for temperature calculation and for normalization, as these typically compare the intensities of spectral lines that may have different spatial distributions in the plasma.

At the plasma center, the observation of high-temperature ionic emissions at early times and low-temperature molecular emissions at later times suggests a strong temperature decrease caused by the rarefaction of the plasma center in the wake of the outgoing shock wave. Instead of being the hottest plasma region as has been commonly

assumed, the center is found to be the coldest plasma region for most of the plasma lifetime, enabling the formation of CaO molecules that are only found at lower temperatures at the same time as ionic and atomic Ca is found in outer hotter regions of the plasma. The observed structure of the plasma plume with a rarefied plasma center and hotter and denser regions closer to the shock wave supports the results of hydrodynamic simulations of the laser-induced plasma in the literature.

The results of this study show that plasma imaging experiments can offer relevant insights for LIBS on Mars. The spatial and temporal separation between different emissions of a single element, as well as the differences in the distributions of emissions related to different elements, underline the complexity of the laser-induced plasma in Martian ambient conditions. For the analysis of Martian LIBS data, a direct consequence is that normalization methods should be carefully chosen so that the spectral features that are to be normalized and the spectral features that are used for the normalization share similar spatiotemporal distributions in the plasma and correspond to similar plasma temperatures. The results of this study seem to indicate that O I is generally better suited for normalization than C I due to being more evenly distributed within the plasma plume. However, it is currently unknown whether this is a general trend or whether it is only the case for samples such as the gypsum that was investigated here. Future plasma imaging studies should therefore investigate the laser-induced plasma produced by different samples in order to understand how the sample composition and matrix effects might influence the observed spatiotemporal distributions of the plasma emissions related to elements in the plasma and in the atmosphere.

6 References

[1] A.K. Knight, N.L. Scherbarth, D.A. Cremers, M.J. Ferris, Characterization of Laser-Induced Breakdown Spectroscopy (LIBS) for Application to Space Exploration, Appl. Spectrosc. 54 (2000) 331–340. https://doi.org/10.1366/0003702001949591.

[2] D.A. Cremers, L.J. Radziemski, Basics of the LIBS Plasma, in: Handb. Laser-Induc. Breakdown Spectrosc., John Wiley & Sons, Ltd, 2006: pp. 23–52. https://doi.org/10.1002/0470093013.ch2.

[3] S. Maurice, R.C. Wiens, M. Saccoccio, B. Barraclough, O. Gasnault, O. Forni, N. Mangold, D. Baratoux, S. Bender, G. Berger, J. Bernardin, M. Berthé, N. Bridges, D. Blaney, M. Bouyé, P. Caïs, B. Clark, S. Clegg, A. Cousin, D. Cremers, A. Cros, L. DeFlores, C. Derycke, B. Dingler, G. Dromart, B. Dubois, M. Dupieux, E. Durand, L. d'Uston, C. Fabre, B. Faure, A. Gaboriaud, T. Gharsa, K. Herkenhoff, E. Kan, L. Kirkland, D. Kouach, J.-L. Lacour, Y. Langevin, J. Lasue, S.L. Mouélic, M. Lescure, E. Lewin, D. Limonadi, G. Manhès, P. Mauchien, C. McKay, P.-Y. Meslin, Y. Michel, E. Miller, H.E. Newsom, G. Orttner, A. Paillet, L. Parès, Y. Parot, R. Pérez, P. Pinet, F. Poitrasson, B. Quertier, B. Sallé, C. Sotin, V. Sautter, H. Séran, J.J. Simmonds, J.-B. Sirven, R. Stiglich, N. Striebig, J.-J. Thocaven, M.J. Toplis, D. Vaniman, The ChemCam Instrument Suite on the Mars Science Laboratory (MSL) Rover: Science Objectives and Mast Unit Description, Space Sci. Rev. 170 (2012) 95–166. https://doi.org/10.1007/s11214-012-9912-2.

[4] R.C. Wiens, S. Maurice, B. Barraclough, M. Saccoccio, W.C. Barkley, J.F. Bell, S. Bender, J. Bernardin, D. Blaney, J. Blank, M. Bouyé, N. Bridges, N. Bultman, P. Caïs, R.C. Clanton, B. Clark, S. Clegg, A. Cousin, D. Cremers, A. Cros, L. DeFlores, D. Delapp, R. Dingler, C. D'Uston, M. Darby Dyar, T. Elliott, D. Enemark, C. Fabre, M. Flores, O. Forni, O. Gasnault, T. Hale, C. Hays, K. Herkenhoff, E. Kan, L. Kirkland, D. Kouach, D. Landis, Y. Langevin, N. Lanza, F. LaRocca, J. Lasue, J. Latino, D. Limonadi, C. Lindensmith, C. Little, N. Mangold, G. Manhes, P. Mauchien, C. McKay, E. Miller, J. Mooney, R.V. Morris, L. Morrison, T. Nelson, H. Newsom, A. Ollila, M. Ott, L. Pares, R. Perez, F. Poitrasson, C. Provost, J.W. Reiter, T. Roberts, F. Romero, V. Sautter, S. Salazar, J.J. Simmonds, R. Stiglich, S. Storms, N. Striebig, J.-J. Thocaven, T. Trujillo, M. Ulibarri, D. Vaniman, N. Warner, R. Waterbury, R. Whitaker, J. Witt, B. Wong-Swanson, The ChemCam Instrument Suite on the Mars Science Laboratory (MSL) Rover: Body Unit and Combined System Tests, Space Sci. Rev. 170 (2012) 167–227. https://doi.org/10.1007/s11214-012-9902-4.

[5] S. Maurice, S.M. Clegg, R.C. Wiens, O. Gasnault, W. Rapin, O. Forni, A. Cousin, V. Sautter, N. Mangold, L.L. Deit, M. Nachon, R.B. Anderson, N.L. Lanza, C. Fabre, V. Payré, J. Lasue, P.-Y. Meslin, R.J. Léveillé, B.L. Barraclough, P. Beck, S.C. Bender, G. Berger, J.C. Bridges, N.T. Bridges, G. Dromart, M.D. Dyar, R. Francis, J. Frydenvang, B. Gondet, B.L. Ehlmann, K.E. Herkenhoff, J.R. Johnson, Y. Langevin, M.B. Madsen, N. Melikechi, J.-L. Lacour, S.L. Mouélic, E. Lewin, H.E. Newsom, A.M. Ollila, P. Pinet, S. Schröder, J.-B. Sirven, R.L. Tokar, M.J. Toplis, C. d'Uston, D.T. Vaniman, A.R. Vasavada, ChemCam activities and discoveries during the nominal mission of the Mars Science Laboratory in Gale crater, Mars, J. Anal. At. Spectrom. 31 (2016) 863–889. https://doi.org/10.1039/C5JA00417A.

[6] ChemCam's laser is back to firing, (n.d.). https://www.lanl.gov/discover/science-briefs/2021/May/0528-chemcam-laser-firing.shtml (accessed July 5, 2021).
[7] V. Sautter, C. Fabre, O. Forni, M.J. Toplis, A. Cousin, A.M. Ollila, P.Y. Meslin, S. Maurice, R.C. Wiens, D. Baratoux, N. Mangold, S.L. Mouélic, O. Gasnault, G. Berger, J. Lasue, R.A. Anderson, E. Lewin, M. Schmidt, D. Dyar, B.L. Ehlmann, J. Bridges, B. Clark, P. Pinet, Igneous mineralogy at Bradbury Rise: The first ChemCam campaign at Gale crater, J. Geophys. Res. Planets. 119 (2014) 30–46. https://doi.org/10.1002/2013JE004472.
[8] R. Anderson, J.C. Bridges, A. Williams, L. Edgar, A. Ollila, J. Williams, M. Nachon, N. Mangold, M. Fisk, J. Schieber, S. Gupta, G. Dromart, R. Wiens, S. Le Mouélic, O. Forni, N. Lanza, A. Mezzacappa, V. Sautter, D. Blaney, B. Clark, S. Clegg, O. Gasnault, J. Lasue, R. Léveillé, E. Lewin, K.W. Lewis, S. Maurice, H. Newsom, S.P. Schwenzer, D. Vaniman, ChemCam results from the Shaler outcrop in Gale crater, Mars, Icarus. 249 (2015) 2–21. https://doi.org/10.1016/j.icarus.2014.07.025.
[9] R.C. Wiens, S. Maurice, M.S. Team, ChemCam: Chemostratigraphy by the First Mars Microprobe, Elements. 11 (2015) 33–38. https://doi.org/10.2113/gselements.11.1.33.
[10] M. Nachon, N. Mangold, O. Forni, L.C. Kah, A. Cousin, R.C. Wiens, R. Anderson, D. Blaney, J.G. Blank, F. Calef, S.M. Clegg, C. Fabre, M.R. Fisk, O. Gasnault, J.P. Grotzinger, R. Kronyak, N.L. Lanza, J. Lasue, L.L. Deit, S.L. Mouélic, S. Maurice, P.-Y. Meslin, D.Z. Oehler, V. Payré, W. Rapin, S. Schröder, K. Stack, D. Sumner, Chemistry of diagenetic features analyzed by ChemCam at Pahrump Hills, Gale crater, Mars, Icarus. 281 (2017) 121–136. https://doi.org/10.1016/j.icarus.2016.08.026.
[11] J. Frydenvang, N. Mangold, R.C. Wiens, A.A. Fraeman, L.A. Edgar, C.M. Fedo, J. L'Haridon, C.C. Bedford, S. Gupta, J.P. Grotzinger, J.C. Bridges, B.C. Clark, E.B. Rampe, O. Gasnault, S. Maurice, P.J. Gasda, N.L. Lanza, A.M. Olilla, P.-Y. Meslin, V. Payré, F. Calef, M. Salvatore, C.H. House, The Chemostratigraphy of the Murray Formation and Role of Diagenesis at Vera Rubin Ridge in Gale Crater, Mars, as Observed by the ChemCam Instrument, J. Geophys. Res. Planets. 125 (2020) e2019JE006320. https://doi.org/10.1029/2019JE006320.
[12] S. Maurice, R.C. Wiens, P. Bernardi, P. Caïs, S. Robinson, T. Nelson, O. Gasnault, J.-M. Reess, M. Deleuze, F. Rull, J.-A. Manrique, S. Abbaki, R.B. Anderson, Y. André, S.M. Angel, G. Arana, T. Battault, P. Beck, K. Benzerara, S. Bernard, J.-P. Berthias, O. Beyssac, M. Bonafous, B. Bousquet, M. Boutillier, A. Cadu, K. Castro, F. Chapron, B. Chide, K. Clark, E. Clavé, S. Clegg, E. Cloutis, C. Collin, E.C. Cordoba, A. Cousin, J.-C. Dameury, W. D'Anna, Y. Daydou, A. Debus, L. Deflores, E. Dehouck, D. Delapp, G. De Los Santos, C. Donny, A. Doressoundiram, G. Dromart, B. Dubois, A. Dufour, M. Dupieux, M. Egan, J. Ervin, C. Fabre, A. Fau, W. Fischer, O. Forni, T. Fouchet, J. Frydenvang, S. Gauffre, M. Gauthier, V. Gharakanian, O. Gilard, I. Gontijo, R. Gonzalez, D. Granena, J. Grotzinger, R. Hassen-Khodja, M. Heim, Y. Hello, G. Hervet, O. Humeau, X. Jacob, S. Jacquinod, J.R. Johnson, D. Kouach, G. Lacombe, N. Lanza, L. Lapauw, J. Laserna, J. Lasue, L. Le Deit, S. Le Mouélic, E. Le Comte, Q.-M. Lee, C. Legett, R. Leveille, E. Lewin, C. Leyrat, G. Lopez-Reyes, R. Lorenz, B. Lucero, J.M. Madariaga, S. Madsen, M. Madsen, N. Mangold, F. Manni, J.-F. Mariscal, J. Martinez-Frias, K. Mathieu, R. Mathon, K.P. McCabe, T. McConnochie, S.M. McLennan, J. Mekki, N. Melikechi, P.-Y. Meslin, Y. Micheau, Y. Michel, J.M. Michel, D. Mimoun, A. Misra, G. Montagnac, C. Montaron, F. Montmessin, J. Moros, V. Mousset, Y. Morizet, N. Murdoch, R.T. Newell, H. Newsom, N. Nguyen Tuong, A.M. Ollila, G. Orttner, L. Oudda, L. Pares, J. Parisot, Y. Parot, R. Pérez, D. Pheav, L. Picot, P. Pilleri, C. Pilorget, P. Pinet, G. Pont, F. Poulet, C. Quantin-Nataf, B. Quertier, D. Rambaud, W. Rapin, P. Romano, L. Roucayrol, C. Royer, M. Ruellan, B.F. Sandoval, V. Sautter, M.J. Schoppers, S. Schröder, H.-C. Seran, S.K. Sharma, P. Sobron, M. Sodki, A. Sournac, V. Sridhar, D. Standarovsky, S. Storms, N. Striebig, M. Tatat, M. Toplis, I. Torre-Fdez, N. Toulemont, C. Velasco, M. Veneranda, D. Venhaus, C. Virmontois, M. Viso, P. Willis, K.W. Wong, The SuperCam Instrument Suite on the Mars 2020 Rover: Science Objectives and Mast-Unit Description, Space Sci. Rev. 217 (2021) 47. https://doi.org/10.1007/s11214-021-00807-w.
[13] R.C. Wiens, S. Maurice, S.H. Robinson, A.E. Nelson, P. Cais, P. Bernardi, R.T. Newell, S. Clegg, S.K. Sharma, S. Storms, J. Deming, D. Beckman, A.M. Ollila, O. Gasnault, R.B. Anderson, Y. André, S. Michael Angel, G. Arana, E. Auden, P. Beck, J. Becker, K. Benzerara, S. Bernard, O. Beyssac, L. Borges, B. Bousquet, K. Boyd, M. Caffrey, J. Carlson, K. Castro, J. Celis, B. Chide, K. Clark, E. Cloutis, E.C. Cordoba, A. Cousin, M. Dale, L. Deflores, D. Delapp, M. Deleuze, M. Dirmyer, C. Donny, G. Dromart, M. George Duran, M. Egan, J. Ervin, C. Fabre, A. Fau, W. Fischer, O. Forni, T. Fouchet, R. Fresquez, J. Frydenvang, D. Gasway, I. Gontijo, J. Grotzinger, X. Jacob, S. Jacquinod, J.R. Johnson, R.A. Klisiewicz, J. Lake, N. Lanza, J. Laserna, J. Lasue, S. Le Mouélic, C. Legett, R. Leveille, E. Lewin, G. Lopez-Reyes, R. Lorenz, E. Lorigny, S.P. Love, B. Lucero, J.M. Madariaga, M. Madsen, S. Madsen, N. Mangold, J.A. Manrique, J.P. Martinez, J. Martinez-Frias, K.P. McCabe, T.H. McConnochie, J.M. McGlown, S.M. McLennan, N. Melikechi, P.-Y. Meslin, J.M. Michel, D. Mimoun, A. Misra, G. Montagnac, F. Montmessin, V. Mousset, N. Murdoch, H. Newsom, L.A. Ott, Z.R. Ousnamer, L. Pares, Y. Parot, R. Pawluczyk, C. Glen Peterson, P. Pilleri, P. Pinet, G. Pont, F. Poulet, C. Provost, B. Quertier, H. Quinn, W. Rapin, J.-M. Reess, A.H. Regan, A.L. Reyes-Newell, P.J. Romano, C. Royer, F. Rull, B. Sandoval, J.H. Sarrao, V. Sautter, M.J. Schoppers, S. Schröder, D. Seitz, T. Shepherd, P. Sobron, B. Dubois, V. Sridhar, M.J. Toplis, I. Torre-Fdez, I.A. Trettel, M. Underwood, A. Valdez, J. Valdez, D. Venhaus, P. Willis, The SuperCam Instrument Suite on the NASA Mars 2020 Rover: Body Unit and Combined System Tests, Space Sci. Rev. 217 (2020) 4. https://doi.org/10.1007/s11214-020-00777-5.

[14] W. Xu, X. Liu, Z. Yan, L. Li, Z. Zhang, Y. Kuang, H. Jiang, H. Yu, F. Yang, C. Liu, T. Wang, C. Li, Y. Jin, J. Shen, B. Wang, W. Wan, J. Chen, S. Ni, Y. Ruan, R. Xu, C. Zhang, Z. Yuan, X. Wan, Y. Yang, Z. Li, Y. Shen, D. Liu, B. Wang, R. Yuan, T. Bao, R. Shu, The MarSCoDe Instrument Suite on the Mars Rover of China's Tianwen-1 Mission, Space Sci. Rev. 217 (2021) 64. https://doi.org/10.1007/s11214-021-00836-5.
[15] D.W. Hahn, N. Omenetto, Laser-Induced Breakdown Spectroscopy (LIBS), Part I: Review of Basic Diagnostics and Plasma–Particle Interactions: Still-Challenging Issues Within the Analytical Plasma Community, Appl. Spectrosc. 64 (2010) 335A-366A.
[16] D.W. Hahn, N. Omenetto, Laser-Induced Breakdown Spectroscopy (LIBS), Part II: Review of Instrumental and Methodological Approaches to Material Analysis and Applications to Different Fields, Appl. Spectrosc. 66 (2012) 347–419.
[17] G. Colonna, A. Casavola, M. Capitelli, Modelling of LIBS plasma expansion, Spectrochim. Acta Part B At. Spectrosc. 56 (2001) 567–586. https://doi.org/10.1016/S0584-8547(01)00230-0.
[18] S.S. Harilal, B.E. Brumfield, M.C. Phillips, Lifecycle of laser-produced air sparks, Phys. Plasmas. 22 (2015) 063301. https://doi.org/10.1063/1.4922076.
[19] G.S. Senesi, Laser-Induced Breakdown Spectroscopy (LIBS) applied to terrestrial and extraterrestrial analogue geomaterials with emphasis to minerals and rocks, Earth-Sci. Rev. 139 (2014) 231–267. https://doi.org/10.1016/j.earscirev.2014.09.008.
[20] C. Aragón, J.A. Aguilera, Characterization of laser induced plasmas by optical emission spectroscopy: A review of experiments and methods, Spectrochim. Acta Part B At. Spectrosc. 63 (2008) 893–916. https://doi.org/10.1016/j.sab.2008.05.010.
[21] S.M. Zaytsev, A.M. Popov, T.A. Labutin, Stationary model of laser-induced plasma: Critical evaluation and applications, Spectrochim. Acta Part B At. Spectrosc. 158 (2019) 105632. https://doi.org/10.1016/j.sab.2019.06.002.
[22] S.V. Shabanov, I.B. Gornushkin, Modeling chemical reactions in laser-induced plasmas, Appl. Phys. A. 121 (2015) 1087–1107. https://doi.org/10.1007/s00339-015-9445-0.
[23] S.V. Shabanov, I.B. Gornushkin, Anions in laser-induced plasmas, Appl. Phys. A. 122 (2016) 676. https://doi.org/10.1007/s00339-016-0175-8.
[24] S.V. Shabanov, I.B. Gornushkin, Chemistry in laser-induced plasmas at local thermodynamic equilibrium, Appl. Phys. A. 124 (2018) 716. https://doi.org/10.1007/s00339-018-2129-9.
[25] J. Hermann, A. Lorusso, A. Perrone, F. Strafella, C. Dutouquet, B. Torralba, Simulation of emission spectra from nonuniform reactive laser-induced plasmas, Phys. Rev. E. 92 (2015) 053103. https://doi.org/10.1103/PhysRevE.92.053103.
[26] A.D. Giacomo, J. Hermann, Laser-induced plasma emission: from atomic to molecular spectra, J. Phys. Appl. Phys. 50 (2017) 183002. https://doi.org/10.1088/1361-6463/aa6585.
[27] P.B. Hansen, S. Schröder, S. Kubitza, K. Rammelkamp, D.S. Vogt, H.-W. Hübers, Modeling of time-resolved LIBS spectra obtained in Martian atmospheric conditions with a stationary plasma approach, Spectrochim. Acta Part B At. Spectrosc. 178 (2021) 106115. https://doi.org/10.1016/j.sab.2021.106115.
[28] A. Bogaerts, Z. Chen, Effect of laser parameters on laser ablation and laser-induced plasma formation: A numerical modeling investigation, Spectrochim. Acta Part B At. Spectrosc. 60 (2005) 1280–1307. https://doi.org/10.1016/j.sab.2005.06.009.
[29] S.V. Shabanov, I.B. Gornushkin, Two-dimensional axisymmetric models of laser induced plasmas relevant to laser induced breakdown spectroscopy, Spectrochim. Acta Part B At. Spectrosc. 100 (2014) 147–172. https://doi.org/10.1016/j.sab.2014.08.026.
[30] J.A. Aguilera, C. Aragón, J. Bengoechea, Spatial characterization of laser-induced plasmas by deconvolution of spatially resolved spectra, Appl. Opt. 42 (2003) 5938–5946. https://doi.org/10.1364/AO.42.005938.
[31] A. De Giacomo, M. Dell'Aglio, R. Gaudiuso, G. Cristoforetti, S. Legnaioli, V. Palleschi, E. Tognoni, Spatial distribution of hydrogen and other emitters in aluminum laser-induced plasma in air and consequences on spatially integrated Laser-Induced Breakdown Spectroscopy measurements, Spectrochim. Acta Part B At. Spectrosc. 63 (2008) 980–987. https://doi.org/10.1016/j.sab.2008.06.010.
[32] L. Mercadier, J. Hermann, C. Grisolia, A. Semerok, Diagnostics of nonuniform plasmas for elemental analysis via laser-induced breakdown spectroscopy: demonstration on carbon-based materials, J. Anal. At. Spectrom. 28 (2013) 1446–1455. https://doi.org/10.1039/C3JA50127B.
[33] L.J. Fernández-Menéndez, C. Méndez-López, C. Alvarez-Llamas, C. González-Gago, J. Pisonero, N. Bordel, Spatio-temporal distribution of atomic and molecular excited species in Laser-Induced Breakdown Spectroscopy: Potential implications on the determination of halogens, Spectrochim. Acta Part B At. Spectrosc. 168 (2020) 105848. https://doi.org/10.1016/j.sab.2020.105848.
[34] A.-M. Harri, M. Genzer, O. Kemppinen, H. Kahanpää, J. Gomez-Elvira, J.A. Rodriguez-Manfredi, R. Haberle, J. Polkko, W. Schmidt, H. Savijärvi, J. Kauhanen, E. Atlaskin, M. Richardson, T. Siili, M. Paton, M. de la T. Juarez, C. Newman, S. Rafkin, M.T. Lemmon, M. Mischna, S. Merikallio, H. Haukka, J. Martin-Torres, M.-P. Zorzano, V.

Peinado, R. Urqui, A. Lapinette, A. Scodary, T. Mäkinen, L. Vazquez, N. Rennó, the R.S. Team, Pressure observations by the Curiosity rover: Initial results, J. Geophys. Res. Planets. 119 (2014) 82–92. https://doi.org/10.1002/2013JE004423.
[35] M.G. Trainer, M.H. Wong, T.H. McConnochie, H.B. Franz, S.K. Atreya, P.G. Conrad, F. Lefèvre, P.R. Mahaffy, C.A. Malespin, H.L.K. Manning, J. Martín-Torres, G.M. Martínez, C.P. McKay, R. Navarro-González, Á. Vicente-Retortillo, C.R. Webster, M.-P. Zorzano, Seasonal Variations in Atmospheric Composition as Measured in Gale Crater, Mars, J. Geophys. Res. Planets. 124 (2019) 3000–3024. https://doi.org/10.1029/2019JE006175.
[36] J. Hermann, C. Gerhard, E. Axente, C. Dutouquet, Comparative investigation of laser ablation plumes in air and argon by analysis of spectral line shapes: Insights on calibration-free laser-induced breakdown spectroscopy, Spectrochim. Acta Part B At. Spectrosc. 100 (2014) 189–196. https://doi.org/10.1016/j.sab.2014.08.014.
[37] J. Hermann, D. Grojo, E. Axente, C. Gerhard, M. Burger, V. Craciun, Ideal radiation source for plasma spectroscopy generated by laser ablation, Phys. Rev. E. 96 (2017) 053210. https://doi.org/10.1103/PhysRevE.96.053210.
[38] C.R. Ytsma, M.D. Dyar, Effects of univariate and multivariate regression on the accuracy of hydrogen quantification with laser-induced breakdown spectroscopy, Spectrochim. Acta Part B At. Spectrosc. 139 (2018) 27–37. https://doi.org/10.1016/j.sab.2017.11.010.
[39] W. Rapin, P.-Y. Meslin, S. Maurice, R.C. Wiens, D. Laporte, B. Chauviré, O. Gasnault, S. Schröder, P. Beck, S. Bender, O. Beyssac, A. Cousin, E. Dehouck, C. Drouet, O. Forni, M. Nachon, N. Melikechi, B. Rondeau, N. Mangold, N.H. Thomas, Quantification of water content by laser induced breakdown spectroscopy on Mars, Spectrochim. Acta Part B At. Spectrosc. 130 (2017) 82–100. https://doi.org/10.1016/j.sab.2017.02.007.
[40] S. Schröder, K. Rammelkamp, D.S. Vogt, O. Gasnault, H.-W. Hübers, Contribution of a martian atmosphere to laser-induced breakdown spectroscopy (LIBS) data and testing its emission characteristics for normalization applications, Icarus. 325 (2019) 1–15. https://doi.org/10.1016/j.icarus.2019.02.017.
[41] B. Chide, S. Maurice, N. Murdoch, J. Lasue, B. Bousquet, X. Jacob, A. Cousin, O. Forni, O. Gasnault, P.-Y. Meslin, J.-F. Fronton, M. Bassas-Portús, A. Cadu, A. Sournac, D. Mimoun, R.C. Wiens, Listening to laser sparks: a link between Laser-Induced Breakdown Spectroscopy, acoustic measurements and crater morphology, Spectrochim. Acta Part B At. Spectrosc. 153 (2019) 50–60. https://doi.org/10.1016/j.sab.2019.01.008.
[42] B. Chide, S. Maurice, A. Cousin, B. Bousquet, D. Mimoun, O. Beyssac, P.-Y. Meslin, R.C. Wiens, Recording laser-induced sparks on Mars with the SuperCam microphone, Spectrochim. Acta Part B At. Spectrosc. 174 (2020) 106000. https://doi.org/10.1016/j.sab.2020.106000.
[43] M. Nachon, S.M. Clegg, N. Mangold, S. Schröder, L.C. Kah, G. Dromart, A. Ollila, J.R. Johnson, D.Z. Oehler, J.C. Bridges, S.L. Mouélic, O. Forni, R.C. Wiens, R.B. Anderson, D.L. Blaney, J.F. Bell, B. Clark, A. Cousin, M.D. Dyar, B. Ehlmann, C. Fabre, O. Gasnault, J. Grotzinger, J. Lasue, E. Lewin, R. Léveillé, S. McLennan, S. Maurice, P.-Y. Meslin, W. Rapin, M. Rice, S.W. Squyres, K. Stack, D.Y. Sumner, D. Vaniman, D. Wellington, Calcium sulfate veins characterized by ChemCam/Curiosity at Gale crater, Mars, J. Geophys. Res. Planets. 119 (2014) 1991–2016. https://doi.org/10.1002/2013JE004588.
[44] P. Stavropoulos, C. Palagas, G.N. Angelopoulos, D.N. Papamantellos, S. Couris, Calibration Measurements in laser-induced breakdown spectroscopy using nanosecond and picosecond lasers, Spectrochim. Acta Part B At. Spectrosc. 59 (2004) 1885–1892. https://doi.org/10.1016/j.sab.2004.08.005.
[45] X. Liu, G. Li, X. Liu, Y. Mu, Y. Wang, P. Ding, Gauss numerical inversion for use in computing the radiation field from a cylindrically symmetric radiation source, Radiat. Phys. Chem. 61 (2001) 93–98. https://doi.org/10.1016/S0969-806X(00)00432-1.
[46] S. Ma, H. Gao, L. Wu, G. Zhang, Abel inversion using Legendre polynomials approximations, J. Quant. Spectrosc. Radiat. Transf. 109 (2008) 1745–1757. https://doi.org/10.1016/j.jqsrt.2008.01.013.
[47] I. B. Gornushkin, S. V. Shabanov, U. Panne, Abel inversion applied to a transient laser induced plasma: implications from plasma modeling, J. Anal. At. Spectrom. 26 (2011) 1457–1465. https://doi.org/10.1039/C1JA10044K.
[48] A.M. El Sherbini, H. Hegazy, Th.M. El Sherbini, Measurement of electron density utilizing the Hα-line from laser produced plasma in air, Spectrochim. Acta Part B At. Spectrosc. 61 (2006) 532–539. https://doi.org/10.1016/j.sab.2006.03.014.
[49] D.S. Vogt, S. Schröder, K. Rammelkamp, P.B. Hansen, S. Kubitza, H.-W. Hübers, CaCl and CaF emission in LIBS under simulated martian conditions, Icarus. 335 (2020) 113393. https://doi.org/10.1016/j.icarus.2019.113393.
[50] M.A. Gigosos, M.Á. González, V. Cardeñoso, Computer simulated Balmer-alpha, -beta and -gamma Stark line profiles for non-equilibrium plasmas diagnostics, Spectrochim. Acta Part B At. Spectrosc. 58 (2003) 1489–1504. https://doi.org/10.1016/S0584-8547(03)00097-1.
[51] N. Konjević, M. Ivković, N. Sakan, Hydrogen Balmer lines for low electron number density plasma diagnostics, Spectrochim. Acta Part B At. Spectrosc. 76 (2012) 16–26. https://doi.org/10.1016/j.sab.2012.06.026.

[52] M. Burger, J. Hermann, Stark broadening measurements in plasmas produced by laser ablation of hydrogen containing compounds, Spectrochim. Acta Part B At. Spectrosc. 122 (2016) 118–126. https://doi.org/10.1016/j.sab.2016.06.005.
[53] Ş. Yalçin, D.R. Crosley, G.P. Smith, G.W. Faris, Influence of ambient conditions on the laser air spark, Appl. Phys. B Lasers Opt. 68 (1999) 121–130. https://doi.org/10.1007/s003400050596.
[54] J.A. Aguilera, C. Aragón, Characterization of a laser-induced plasma by spatially resolved spectroscopy of neutral atom and ion emissions.: Comparison of local and spatially integrated measurements, Spectrochim. Acta Part B At. Spectrosc. 59 (2004) 1861–1876. https://doi.org/10.1016/j.sab.2004.08.003.
[55] A. Kramida, Yu. Ralchenko, J. Reader, NIST Atomic Spectra Database (version 5.8), (2021). https://physics.nist.gov/asd (accessed July 13, 2021).
[56] B. deB Darwent, Bond Dissociation Energies in Simple Molecules, NATIONAL STANDARD REFERENCE DATA SYSTEM, 1970. https://apps.dtic.mil/sti/citations/ADD095293 (accessed July 13, 2021).